Zeolite collapse and polyamorphism

2007 J. Phys.: Condens. Matter 19 415102

(http://iopscience.iop.org/0953-8984/19/41/415102)

IOP PUBLISHING JOURNAL OF PHYSICS: CONDENSED MATTER

J. Phys.: Condens. Matter **19** (2007) 415102 (17pp) doi:10.1088/0953-8984/19/41/415102

Zeolite collapse and polyamorphism

G Neville Greaves[1], F Meneau[1,2], F Kargl[1], D Ward[1], P Holliman[3] and F Albergamo[4]

[1] Centre for Advanced Functional Materials and Devices, Institute of Mathematical and Physical Sciences, University of Wales, Aberystwyth, Aberystwyth SY23 3BZ, UK
[2] SOLEIL, Orme des Merisiers, Bâtiment A, Saint Aubin, BP 48, 91192, Gif sur Yvette Cedex, France
[3] College of Physical and Applied Sciences, University of Wales, Bangor, Bangor LL57 2UW, UK
[4] European Synchrotron Radiation Facility, BP 220, 38043 Grenoble Cedex, France

Received 31 May 2007, in final form 31 July 2007
Published 27 September 2007
Online at stacks.iop.org/JPhysCM/19/415102

Abstract

The phenomenology of zeolite collapse is outlined, drawing on recent synchrotron x-ray diffraction experiments and computer simulations of low density cage structures like zeolite A and zeolite Y. Attention is drawn to the importance of polyamorphism in destabilizing this type of microporous crystal and its role in order–disorder as well as amorphous–amorphous transitions, together with associated differences in entropy and density between polyamorphic phases and the precursor zeolite. Magic angle spinning NMR and inelastic x-ray scattering are used to highlight changes in structural order and mechanical rigidity between the starting zeolite and the final high density polyamorph. In conclusion, two-level systems detected with inelastic neutron scattering are described and their involvement in dictating the dynamics of the collapse of zeolitic cage structures.

(Some figures in this article are in colour only in the electronic version)

1. Introduction

Interest in the collapse of low density zeolites, which started from understanding how their functionality as heterogeneous catalysts could be prolonged or regenerated in industrial applications [1–3] and developed into the possible use of microporous materials as precursors for novel ceramics [4–6], is now attracting increasing attention in providing model systems for exploring the various transitions [7–15] that lie at the heart of amorphization—the solid state conversion of crystalline into amorphous materials [16–18]. In many cases, and zeolite collapse is no exception, amorphization is compressive and at ambient temperatures results in negative melting curves, i.e. $\mathrm{d}T/\mathrm{d}P < 0$. Experimentally amorphization of zeolites can be tracked through *in situ* x-ray diffraction [6, 19], small angle x-ray scattering [7], Raman spectroscopy [14] and inelastic neutron scattering [20]. Computer modelling is also emerging as a powerful probe of the structural and dynamic processes occurring during

zeolite collapse [12, 13] and, more importantly, the various phase transitions that mediate the compression of microporous crystals into glasses of the same composition [15].

Evidence for the involvement of polyamorphism in these transformations has also been identified in experiments [7, 14] and recently in computer simulations [15]. Polyamorphism relates to the occurrence of more than one amorphous phase with the same chemical composition but differing in density and entropy [21]—often a low density amorphous (LDA) phase of low entropy and a high density amorphous (HDA) phase of higher entropy. The coexistence of polyamorphic phases has been proposed by Ponyatovsky and Barkolov [22] as the source of instability driving amorphization in many crystalline systems like tetrahedral semiconductors and also hexagonal ice. Indeed we have found reasonable agreement between this model and experiment where the collapse of cage-like zeolites are concerned [7]. In particular the two phase transitions critical to zeolite amorphization are the order–disorder zeolite–LDA transition and the liquid–liquid LDA–HDA transition. Whilst the structure and physical properties of the starting zeolite [1] and final HDA glass [23] are well known, those of the intermediate LDA phase are not. We have referred to the LDA phase as an example of a 'perfect glass' [23]—*vide infra*.

We begin this paper in section 2 with a short introduction to the crystalline, glassy and supercooled states, the microporous structure of zeolites, and the regime of negative melting curves. In section 3 we go on to demonstrate the complementarity of experimental probes of zeolite collapse [7] with recent computational modelling results on cage-like zeolites [15]. In particular, we describe how a simple construction from the measured negative low temperature melting curve and its limits can be used to align the zeolite–LDA and liquid–liquid LDA–HDA phase transitions predicted by 0 K calculations, as well as the evidence for reversibility—low temperature recrystallization—via negative pressures. From this approach estimates of differences in molar volume and entropy between the various crystalline and amorphous phases can be quantified, and can also shed light on the *decompressive* processes observed in the initial zeolite–LDA transition. We go to show in section 4 how new magic angle spinning NMR (MASNMR) and inelastic x-ray scattering data can be used to track structural ordering and mechanical rigidity in the zeolite and HDA phases. In section 5 we discuss the role of THz librational processes in promoting the different phase transitions that convert the periodic structure of a zeolite into the aperiodic structure of a high density disordered glass. Finally in section 6 we conclude with a summary of the factors affecting thermal amorphization zeolites, contrasting these with the amorphization of denser minerals.

2. Melting and amorphization

Amorphization lies at the intersection between the crystalline, liquid and glassy states [23]. Figure 1(a) illustrates the differences in entropy between the three states if local structure is similar. The vibrational entropy is shown by the dashed curve followed by the crystal. At the melting point T_m this increases by $\Delta H_{fusion}/T_m = S_{config}$ for normal melting, where ΔH_{fusion} is the heat of fusion resulting from the enlarged configurational variety enabled by diffusional motion when this reaches the timescale of vibrational dynamics. On supercooling below T_m, T_c marks the cross over from ergodic to non-ergodic behaviour predicted by mode coupling theory [24], where slowing diffusional motion becomes more protracted than the fast vibrational processes common to the liquid and the supercooled state. As the temperature falls still further, the increasing structural relaxation time is eventually overtaken by the cooling process, the glass transition, T_g, is reached and the supercooled liquid is deemed a solid. Throughout supercooling the difference in entropy that separates the liquid from the crystalline state, S_{config}, decreases. With slower cooling rates T_g and with it S_{config} will reduce until, in

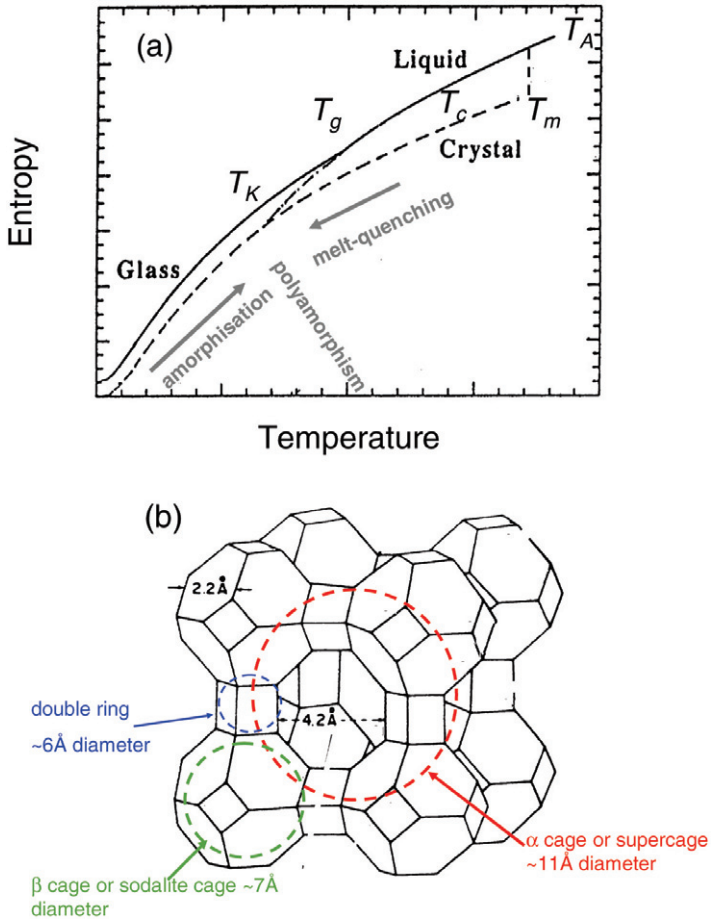

Figure 1. (a) Schematic variation of entropy with temperature for a glass and the corresponding liquid (solid curve) and crystalline phase (dashed curve). The difference between the two curves defines the configurational entropy, S_{config}, which decreases through the supercooled state. The temperatures T_A, T_c, T_g and T_K relate respectively to the ergodic liquid, the crossover from ergodic to non-ergodic behaviour (the critical temperature of mode coupling theory [24]), the glass transition (where the viscosity crosses 10^{12} Pa s) and the Kauzmann temperature (where the entropies of the glass and crystal are equal) [23]. (b) The microporous structure of zeolite A, showing the secondary building units (SBUs): the α cage, β cage and double fourfold ring (D4R). The openings for the α and β cages are indicated. The corners of the SBU polyhedra define the positions of Si and Al tetrahedra and the edges the bridging oxygens. In the regular structure tetrahedral angles are 109.6° and oxygen bridges 144° [1].

principle at a finite glass transition temperature T_K, S_{config} would disappear and a glass with vibrational entropy equal to that of the crystal would result [25]. In practice recrystallization intervenes before the ordered glass predicted by Kauzmann can be formed.

By considering the rheology of collapse we have proposed that zeolite amorphization could offer a more practical route to an ordered or 'perfect glass' than melt-quenching, by approaching the glass transition from the crystalline state [7]. In particular we have identified the perfect glass with the intermediate LDA phase formed prior to the final HDA phase of conventional density [23]. In the Ponyatovsky model [22] polyamorphism is inherent in the amorphization process, as figure 1(a) illustrates. It is also the case that, in

systems like yttria–alumina where polyamorphism has been identified [21, 23], an LDA phase can only be recovered from a liquid–liquid HDA–LDA transition by very rapid quenching from the supercooled state. Accordingly the quenching and amorphization approaches to the polyamorphic regime identified in figure 1(a) are not equivalent. The virtue of the amorphization route is that a perfect glass might be reached from a zeolite–LDA transition if the liquid–liquid LDA–HDA transition can be avoided.

2.1. Structure and density of zeolites

Zeolites share the general formula $M_{x/m}$ $Al_xSi_{s-x}{\cdot}nH_2O$, where M^{m+} is the charge-compensating cation for tetrahedral AlO_4^+ units in the open framework. Typically $0 \leqslant x \leqslant 1$ and AlO_4^+ and SiO_4 tetrahedra are linked throughout by bridging oxygens to create a completely compensated alumino-silicate network [1, 23]. This is illustrated in figure 1(b) for Na-zeolite A for which $x = 1$. The low density cage structure results from the stacking together of large polyhedral units namely sodalite β-cages and double fourfold rings (D4R). Together these generate the even larger 26-hedra α-cages that characterize the low density zeolites. Na-zeolite Y where $x \sim 0.4$, which is also discussed in this paper, has a similar structure with the same β-cages but with double sixfold rings (6DR) replacing the D4R in figure 1(b) creating slightly larger α-cages [1].

The bridging oxygen angle in zeolitic structures is generally around the 144° value found in most silicate and alumino-silicate minerals but which, in the low density zeolite geometry, may promote buckling under compression and potentially some dilation under decompression via rotations of tetrahedra with respect to the common bridging oxygen. This may lie behind the discovery of different cubic phases of Na-zeolite A under pressure in the early classic crystallographic studies of Hazen [26] and, more recently, in the 0 K *ab initio* computer simulations of zeolite structures under positive and negative pressure by Peral and Íñiguez [15], who report transitions characterized by rigid rotations of tetrahedral units. Moreover, the microporous geometry of zeolites (figure 1(b)) shares some similarity with the macrostructure of cellular solids like rigid foams which exhibit *negative* Poisson ratios related to their re-entrant honeycomb structures [27]. Whilst the majority of solids have positive Poisson ratios, swelling laterally under compression, negative Poisson ratio or auxetic materials like foams become fatter in cross-section when stretched. Zeolitic materials may possibly therefore exhibit auxetic behaviour at the single-crystal level. In particular we do not expect their density and compressibility during compression to scale in a simple fashion as amorphization advances.

The molar volume of zeolite Y is plotted in figure 2 with progressive amorphization—amorphization being $1 - x$, where x is the fraction of zeolite remaining, as judged from the strength of the residual diffraction pattern [7, 8]. The data in figure 2 were assembled from the known (crystallographic) density of the zeolite and the Archimedean density of the HDA glass, together with the density of partially amorphized material measured from the mass of a fixed volume allowing for particulate packing. The overall volume change, $\Delta V_A = V_{HDA} - V_{zeolite}$, a fall of 34% at ambient pressure occurs gradually from the start but changes rapidly close to the finish. If the initial fall is due to the zeolite–LDA transition and the final drop due to the LDA–HDA transition then the LDA phase is closer in density to the HDA phase than to the zeolite (figure 2).

2.2. Negative melting curves and polyamorphism

Classically the variation of the melting temperature, T_m, with pressure—the melting curve—is predicted by the Clausius–Clapeyron relation:

$$\frac{dT}{dP} = \frac{\Delta V}{\Delta S}. \tag{1}$$

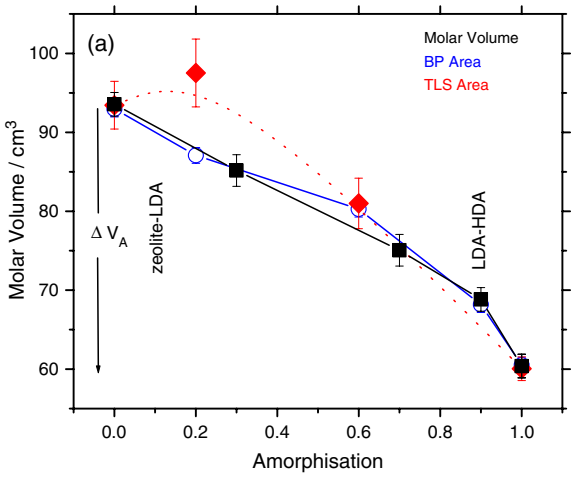

Figure 2. (a) The change in molar volume (■) with the amorphization of Na zeolite Y (FAU), $Na_{56}Al_{56}Si_{136}O_{384}$. The overall volume change, $\Delta V_A = V_{HDA} - V_{zeolite}$, is indicated, together with the positions expected for the zeolite–LDA and LDA–HDA transitions. Relationships between the molar volume and the strengths of low frequency modes during amorphization of Na zeolite Y are also shown. As the molar volume falls the TLS peak at 1.8 meV (◇) from figure 8(a) decreases along with the boson peak (○) from figure 8(b).

This defines first order phase transitions which in crystalline materials are themselves identified by abrupt changes in density and entropy. For the case of melting equation (1) follows the free energy boundary where liquid (L) and crystalline (C) phases coexist. $\Delta V = \Delta V_m = V_L - V_C$ and $\Delta S = \Delta S_m = S_L - S_C$ are the respective differences in molar volume and entropy—where molar in the present context refers to $Na_xAl_xSi_{2-x}O_4$ equivalent. Simple close-packed materials like metals and alkali halides expand on melting at ambient pressure and become disordered, so ΔV_m and ΔS_m are both positive as is the slope of the melting curve, $\frac{dT_m}{dP}$.

Not all melting curves are positive, which is famously the case for ice where $\Delta V_m < 0$ and $\Delta S_m > 0$ and therefore from equation (1) $\frac{dT_m}{dP} = \frac{\Delta V_m}{\Delta S_m} < 0$. This lies at the heart of the physics of crystalline, supercooled and glassy water [28, 29] which was strongly influenced by the ground-breaking experiments of Mishima and colleagues who showed how the low temperature hexagonal phase of ice could be amorphized to a glass at 77 K under 1 GPa of compression—the critical T–P point intersecting the extrapolated negative melting curve [30]. Moreover, by reducing the pressure a second glassy phase was discovered together with a reversible first order 'liquid–liquid' phase transition between the two namely: from a high density HDA phase to a low density LDA phase [31]. In addition to the difference in molar volume between these two glassy states or polyamorphs, $\Delta V_{L-L} = V_{HDA} - V_{LDA}$, a difference in entropy, $\Delta S_{L-L} = S_{HDA} - S_{LDA}$, is also expected—the LDA phase being the more ordered. Accordingly, a decompressive HDA–LDA liquid–liquid phase transition should be exothermic, with a stepwise decrease in density and entropy. Returning to equation (1), if $\Delta V = V_{LDA} - V_{HDA} > 0$ and $\Delta S = S_{LDA} - S_{HDA} < 0$ the characteristic temperature of this transition will fall with increasing pressure, like the melting curve of ice, but now originating below T_m from a critical point in the supercooled region [29].

3. Zeolite collapse

This background of crystalline destabilization under thermobaric stress [16, 28] has proved important in understanding the collapse of zeolites like A and Y [7, 8]. The total volume

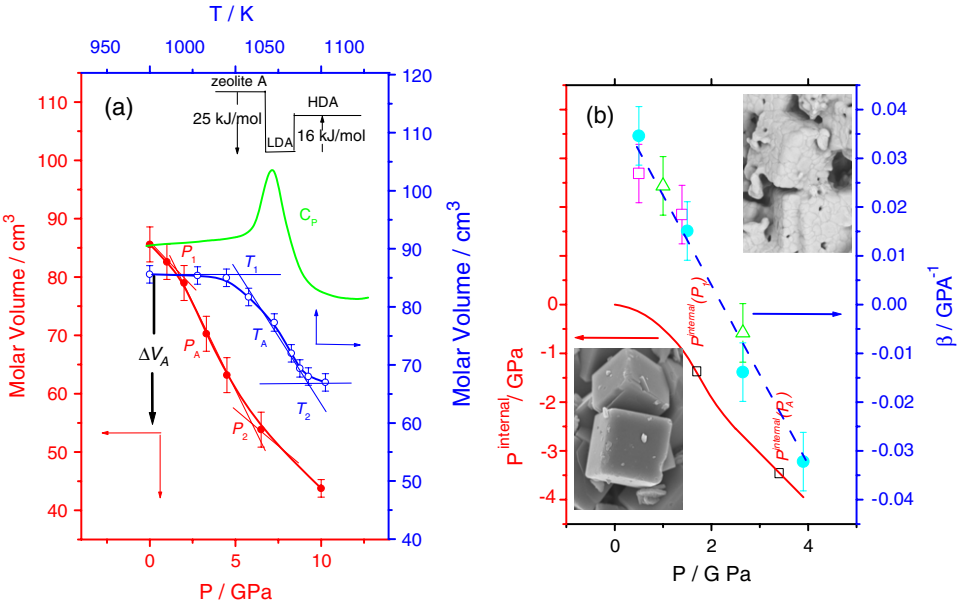

Figure 3. Amorphization of zeolite A (LTA), $Na_{12}Al_{12}Si_{12}O_{48}$. (a) Stepwise decrease in volume $\Delta V_A = V_{HDA} - V_{zeolite}$ under a pressure ramp of 1 MPa s^{-1} (left) and temperature ramp of 30 mdeg s^{-1} (right), molar volume being referenced to $NaAlSiO_4$ equivalent. T_1 and P_1 define the start of microporous collapse and T_2 and P_2 the completion of amorphization, whilst T_A and P_A define the turning points. These temperatures and pressures are used to identify the boundaries between zeolite, LDA and HDA phases in figure 4. Data adapted from [7]. A DTA scan is also included together with the enthalpy changes ΔH taken from [34] for zeolite A, nepheline/LDA and the high density glass (HDA). (b) Dependence of macroscopic compressibility β (right) and the internal pressure, $P^{internal}$, (left) on applied hydrostatic pressure during compressive amorphization measured from the zeolite diffraction pattern. $P^{internal}$ is increasingly negative, explaining the cavitation observed in the micrographs of zeolite crystals before and during amorphization [9]. $P^{internal}(T)$ and $P^{internal}(P)$ values refer to the internal pressures in the residual zeolite (obtained from (b)) encountered temporarily in ramping under temperature or under pressure. Inset: micrographs of starting zeolite A (left) and after partial amorphisation (right).

change ΔV_A on compressive amorphization illustrated in figure 2 occurs over a fairly narrow range of temperatures or pressures. Results for zeolite A from [7] are recompiled in figure 3(a). For instance, at ambient temperature, T_{RT}, this zeolite collapses around 4 GPa (P_A) and at ambient pressure, P_{RP}, at around 1050 K (T_A), defining the 'negative amorphization curve' T_A, P_{RP}–T_{RT}, P_A shown in figure 4(a).

However, the low temperature melting of cage-like zeolites turns out to be more subtle than dT_A/dP_A simply being negative. In particular, we have argued that the negative T_A–P_A curve defines the liquid–liquid transition between LDA and HDA phases [7–9, 32] as figures 3 and 4 illustrate. Looking at this in more detail, the negative T_A–P_A curve is surrounded by the limits that define ΔV_A. These are identified in figure 3(a) by T_1 and P_1 where collapse commences, and by T_2 and P_2, where amorphization is complete. Adding these to the T–P diagram in figure 4(a) establishes experimental boundaries for a zone of instability either side of the negative amorphization line T_A, P_{RP}–T_{RT}, P_A, T_1, P_{RP}–T_{RT}, P_1 defining the thermobaric limits for zeolite stability and T_2, P_{RP}–T_{RT}, P_2 the limits beyond which vitrification appears irreversible over periods of weeks.

In the Ponyatovsky–Barkalov model for compressive amorphization [22], the LDA–HDA liquid–liquid phase transition between the low and high density phases that are believed to

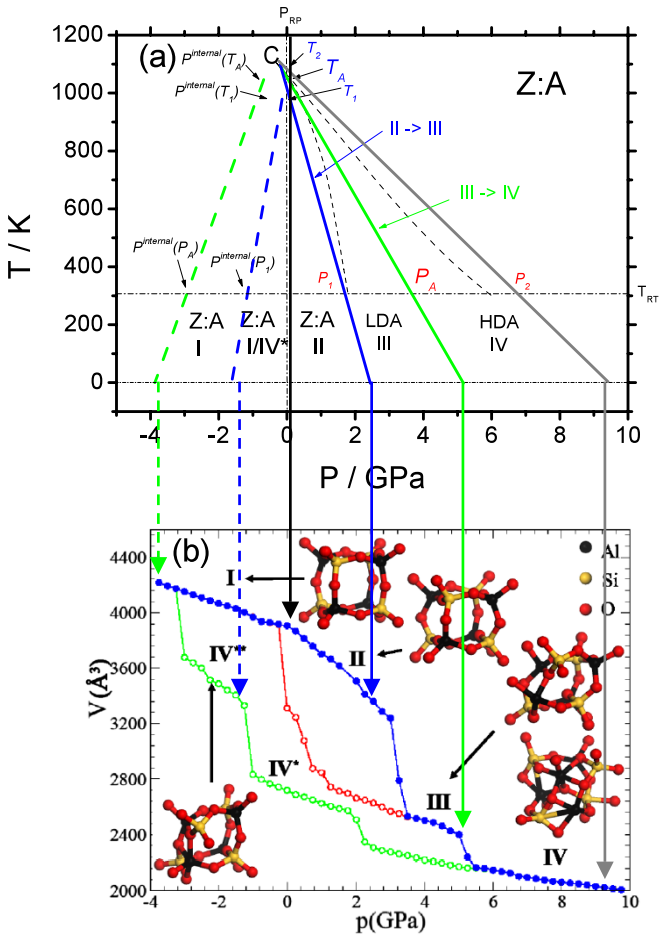

Figure 4. Comparison between the various thresholds in the collapse of zeolite A. (a) Upper frame: experiment [7, 9, 23]. The limits T_1, P_1, T_2, P_2, T_A and P_A for thermal and pressure induced amorphization are taken from figure 3(a). The dashed lines are the spinodal limits calculated from the model of Ponyatovsky and Barkolov [22]. The zeolite–LDA transition defined by $T_1\,P_{RP}$–T_{RT}, P_1 is shown by the solid blue line and the LDA–HDA transition $T_A\,P_{RP}$–T_{RT}, P_A by the solid green line. The dashed blue line at negative pressures relates to *decompression* at the start of collapse at T_{RT}, $P^{internal}(P_1)$ and T_1, $P^{internal}(T_1)$ and the dashed green line to decompression at the turning point T_{RT}, $P^{internal}(P_A)$ and T_A, $P^{internal}(T_A)$—both obtained from the internal pressures derived from figure 3(b). (b) Lower frame: *ab initio* MD 0 K computer simulations of volume versus pressure [15]. First order discontinuous transitions II–III and III–IV are reversible via III–I and V*–IV** respectively to the reference zeolite I. The vertical arrows in (b) follow extrapolations of the experimental data to 0 K in (a) and associate the zeolite at positive pressure and the amorphous LDA and HDA phases with II, III, and IV, respectively.

destabilize the periodic lattice is defined by equation (1), namely

$$\frac{dT_A}{dP_A} = \frac{\Delta V_{L-L}}{\Delta S_{L-L}} \tag{2}$$

$\Delta S_{L-L} = S_{HDA} - S_{LDA} > 0$ and $\Delta V_{L-L} = V_{HDA} - V_{HDA} < 0$, so $dT_A/dP_A < 0$. The negative amorphization curve is bounded by the spinodal limits defined by $d^2G/dc^2 = 0$, where c, for example, is the concentration of the LDA phase [23, 32]. These limits for the LDA and

HDA phases are shown by the dashed lines in figure 4(a) and are in reasonable alignment with the experimental T_1, P_{RP}–T_{RT}, P_1 and T_2, P_{RP}–T_{RT}, P_2 boundaries for instability determined experimentally [7]. In the future it will be interesting to measure zeolite collapse at elevated temperatures *and* pressures in order to examine the degree to which the T_A, P_{RP}–T_{RT}, P_A amorphization curve and its boundaries are curved.

3.1. Displacive and disordering first order phase transitions

Figure 4 also includes important new *ab initio* 0 K computer simulations which model amorphization processes in zeolites as a sequence of first order phase transitions induced by compression but also by decompression [15]. In particular, with increasing pressure, these calculations reveal a displacive *order–disorder* transition (marked II–III) close to 3 GPa. This is identified by an abrupt decrease in volume and is found to be associated with a narrowing of the Si–O–Al bridging angle [15]. In all other respects, though, the crystalline (II) and the amorphous (III) phase are topologically equivalent. However, the phase transition is found to be reversible, albeit with hysteresis (red curve in figure 4(b)). Interestingly this first order transition lies close to our experimental T_1, P_{RP}–T_{RT}, P_1 line if this is extrapolated to 0 K. We therefore associate zeolite A at ambient pressure with Peral and Íñiguez' phase II and our LDA phase with their amorphous phase III. Moreover the initial abrupt fall in molar volume observed experimentally (figure 3(a)), which we have previously interpreted as being due to the microporous zeolite transforming into an ordered LDA phase [8], is borne out in the displacive nature of the first order phase transition between the crystalline phase II and amorphous phase III in these computer simulations (figure 4(b)) [15].

At higher pressures of around 5 GPa the 0 K simulations reveal a subsequent first order *amorphous–amorphous* transition, III–IV, which is also topologically disordering. At this point the double fourfold rings—the smallest of the secondary building units of the zeolite A structure shown in figure 1(b)—collapse with a further reduction in the bridging oxygen bond angle [15]. The III–IV transition is also reversible but the hysteresis bypasses the amorphous phase III, eventually recovering the reference zeolite close to −4 GPa (green curve in figure 4(b)). Our experimental negative amorphization T_A–P_A curve extrapolated to 0 K falls close to this disordering III–IV transition, from which we can associate our HDA phase with the topologically disordered phase IV simulated at high pressure. Experimentally the HDA phase has been followed to pressures of 10 GPa, at which point (T_{RT}, P_2) all of the zeolite is fully amorphized [7].

3.2. Identifying the elements of polyamorphism

An exciting outcome of the *ab initio* simulations [15] is that, not only are the zeolite–LDA and LDA–HDA transitions analysed from experiment (figure 4(a)) [7] replicated (figure 4(b)), but also these are abrupt in the 0 K calculations and well separated thermodynamically. In particular the LDA or phase III shares the topology of the zeolite. We have already drawn attention to fact that the LDA phase might be a perfect glass [7, 8, 10, 23], equivalent to the ideal melt-quenched glass predicted by Kauzmann [25] shown schematically in figure 1(a) with a glass transition temperature T_K. On the other hand alumino-silicate melts at conventional temperatures ($T > T_K$)—HDA in the present terminology—are liquid feldspars and, for many of these, the configurational entropy difference between the supercooled state and the crystalline state, S_{config}, (figure 1(a)) has been measured e.g. [33]. Accordingly, if LDA is a perfect glass, we might reasonably equate its entropy, S_{LDA}, with that of the corresponding feldspar crystal, in which case $S_{config} = S_{HDA} - S_{LDA} = \Delta S_{L-L}$. Turning now to Ponyatovsky

and Barkolov's adaptation of the Clausius–Clapeyron relation (equation (2)), the difference in volume between the HDA and LDA phases, $\Delta V_{\mathrm{L-L}} = V_{\mathrm{HDA}} - V_{\mathrm{LDA}}$ should be given by equation (2) namely,

$$\Delta V_{\mathrm{L-L}} = \Delta S_{\mathrm{L-L}} \frac{\mathrm{d}T_{\mathrm{A}}}{\mathrm{d}P_{\mathrm{A}}}.$$

For Na-zeolite A the corresponding feldspar is nepheline, $NaAlSiO_4$, for which the measured value of S_{config} is 15 J mol^{-1} K^{-1} [33]. Setting this equal to $\Delta S_{\mathrm{L-L}}$ and taking the slope of the negative amorphization curve from figure 4(a) $\frac{\mathrm{d}T_{\mathrm{A}}}{\mathrm{d}P_{\mathrm{A}}}$ (-2×10^{-7} K Pa^{-1}) gives a value of $\Delta V_{\mathrm{L-L}} = V_{\mathrm{HDA}} - V_{\mathrm{LDA}}$ of 3 cm^3 mol^{-1}. This is 12% of $\Delta V_{\mathrm{A}} = V_{\mathrm{HDA}} - V_{\mathrm{zeolite}}$, the total volume change with amorphization (figure 3(a)) and is in reasonable agreement with Peral and Íñiguez' 0 K calculations (figure 4(b)), where $V_{\mathrm{IV}} - V_{\mathrm{IIIV}}$ is 14% of the total volume change between the ambient zeolite phase II and the topologically disordered phase IV. Incidentally the increase in entropy between the LDA and HDA phases, $\Delta S_{\mathrm{L-L}} = S_{\mathrm{HDA}} - S_{\mathrm{LDA}}$, can be identified experimentally by the endothermic step in C_{P} illustrated for zeolite A in figure 3(a) [7].

3.3. Evidence for decompression during zeolite collapse

We turn next to the unusual $T-P$ behaviour in the collapse of cage-like zeolites that occurs at negative pressures (figure 4(a)) where the MD calculations indicate the reversibility of the amorphization processes (figure 4(b)) [15]. Experimentally we find that thermal collapse is accompanied by a sharp negative swing in the expansion coefficient of the residual crystalline fraction whilst pressure induced collapse is accompanied by a lowering in the compressibility [7]—in either case the remaining zeolite is stretched, signifying *negative internal pressures*, P^{internal}. The fall-off in compressibility, β, is shown in figure 3(b) for the pressure induced collapse of zeolite A [7]. These *decompressive* effects apply at the rates of temperature and pressure *increase* given in figure 3(a) [7] and are related to the initial processes of amorphization, becoming less prominent when these are slower. Dramatic evidence for decompression can be seen in micrographs of recovered partially amorphized material [10] illustrated by the insets in figure 3(b).

In the model of Cohen *et al* [18] for displacive amorphization, long range order is destroyed because domain nucleation overwhelms growth. If amorphous nucleation centres are higher in density than the precursor crystal and randomly distributed, then intervening periodic zones should suffer decompression on average. For a given external pressure, the internal pressure, P^{internal}, can be estimated from the difference in compressibility β with the ambient value (figure 3(b)).

This reaches $P^{\mathrm{internal}}(P_1)$ at P_1, the point at which collapse starts to accelerate (figure 3(a)), falling further to $P^{\mathrm{internal}}(P_{\mathrm{A}})$ by the time the ruby calibrant in the diamond anvil cell has reached P_{A} and the LDA–HDA transition has been reached [9]. The internal pressures, P^{internal}, are also plotted in figure 3(b) and are increasingly negative with increasing applied pressure. In a similar way, for temperature induced collapse, the observed negative thermal expansion coefficient [7] combined with the ambient compressibility, β enable the negative internal pressure in the residual crystalline fraction to be estimated, attaining $P^{\mathrm{internal}}(T_1)$ at T_1 and $P^{\mathrm{internal}}(T_{\mathrm{A}})$ at T_{A}. These negative internal pressures at the start of collapse—T_{RT}, $P^{\mathrm{internal}}(P_1)$ and T_1, $P^{\mathrm{internal}}(T_1)$—and at the turning point—T_{RT}, $P^{\mathrm{internal}}(P_{\mathrm{A}})$ and T_{A}, $P^{\mathrm{internal}}(T_{\mathrm{A}})$—are shown connected by the dashed blue and green lines respectively in figure 3(a). Extrapolated to 0 K they extend over reference I in the computer simulations for negative pressures in figure 3(b), together with the phases IV* and IV** related to decompressive hysteresis from the high pressure phase IV [15]. Because experimentally thermobaric stress is applied sequentially, we conclude that the zeolite–LDA transition is progressively achieved through a process of

compression and decompression followed by recompression, until full transformation to the LDA phase (III) is achieved. As we have argued earlier [7, 23], the dynamics of zeolite collapse should therefore be controlled by the viscosity of the LDA phase, as it is gradually accumulated.

Thermally induced zeolite collapse to the LDA phase is accompanied by a sharp exotherm in C_P which anticipates the endothermic step associated with the LDA–HDA transition illustrated in figure 3(a) for zeolite A. The exothermal character of zeolite amorphization, which contrasts with the endothermic character of classical melting, suggests that the zeolite has a *higher* enthalpy than the amorphous phase it transforms into. The enthalpies of anhydrous zeolites, glasses and feldspar crystals have been meticulously catalogued by Navrotsky and Tian in a comprehensive study and indeed decrease in that order [34]. Moreover, within pure silica zeolites the enthalpy difference compared to quartz increases monotonically with molar volume and other density-related properties, like Si–Si non-bonded distances as well as loop configurations [35]—all of which points to the most open framework zeolites like A (LTA) and Y (FAU) being the zeolites likely to amorphize rather than melt and also the ones to exhibit the most prominent exotherm. To this should be added very recent work on Li and Na zeolite beta (BEA), both of which amorphize exothermically between 1000 and 1200 K [36].

Setting the enthalpy of the LDA phase of zeolite A equal to that of nepheline (see section 3.2), the different enthalpies for zeolite A, nepheline/LDA and HDA taken from [34] are sketched in figure 4(a), leading to a drop, $\Delta H = H_{\mathrm{LDA}} - H_{\mathrm{zeolite}}$, of 25 kJ mol^{-1} for the zeolite–LDA transition. Taking the average decompression, $\overline{\Delta P} = (P^{\mathrm{internal}}(T_1) + P^{\mathrm{internal}}(T_A))/2$, for thermal amorphization of 0.3 GPa in figure 4(a) and the mean molar volume for the zeolite–LDA system, $\overline{V} = [2V_{\mathrm{zeolite}} - \Delta V_A + \Delta V_{L-L}]/2$, of 78 cm^3 in figure 3(a), $\overline{V}\,\overline{\Delta P}$ falls through 23 kJ mol^{-1}. This is approximately equal to ΔH for the zeolite–LDA or II–III transition. Given that $\Delta H = T\Delta S + V\Delta P$, in the present context this should approximate $T_1 \Delta S_{\mathrm{LDA-zeolite}} + \overline{V}\,\overline{\Delta P}$, which suggests that $\Delta S = S_{\mathrm{LDA}} - S_{\mathrm{zeolite}} \approx 0$. Little entropy difference between the zeolite and LDA phases is entirely consistent with the displacive nature of the II–III transition reported by Peral and Íñiguez [15] and the 'perfect glass' label that we have used for the thermodynamic character of the LDA phase [23].

4. Structural ordering and mechanical rigidity

Chemical order in tetrahedral alumino-silicate networks is generally achieved by the avoidance of Al–Al contacts which is expressed in Lowenstein's rule [37]. When Si/Al $>$ 1 complete avoidance will result in five Si tetrahedral configurations: Si(0Al), Si(1Al), Si(2Al), Si(3Al) and Si(4Si), and one Al tetrahedral configuration: Al(4Si).

4.1. ^{29}Si

Zeolites display approximate Lowensteinian order as figure 5(a) illustrates with the ^{29}Si MASNMR spectrum for zeolite Y [32]. With chemical shifts, δ, ranging from -87 to -108 ppm, the proportions of each configuration given by the NMR intensities, $I_{\mathrm{Si}(n\mathrm{Al})}$, enable the Si:Al ratio to be obtained from,

$$\frac{\mathrm{Si}}{\mathrm{Al}} = \frac{\sum_{n=0}^{n=4} I_{\mathrm{Si}(n\mathrm{Al})}}{\sum_{n=0}^{n=4} 0.25n I_{\mathrm{Si}(n\mathrm{Al})}}$$

based on chemical order [38]. The MASNMR data for zeolite Y give a Si/Al ratio of 2.3, close to the chemical composition value of 2.4 for $Na_{56}Al_{56}Si1_{136}O_{384}$. The ^{29}Si MASNMR spectrum for the equivalent HDA glass is plotted in figure 5(b) [32], where the resonances from individual Si(nAl) configurations merge into a single broad peak. The weighted average width (FWHM)

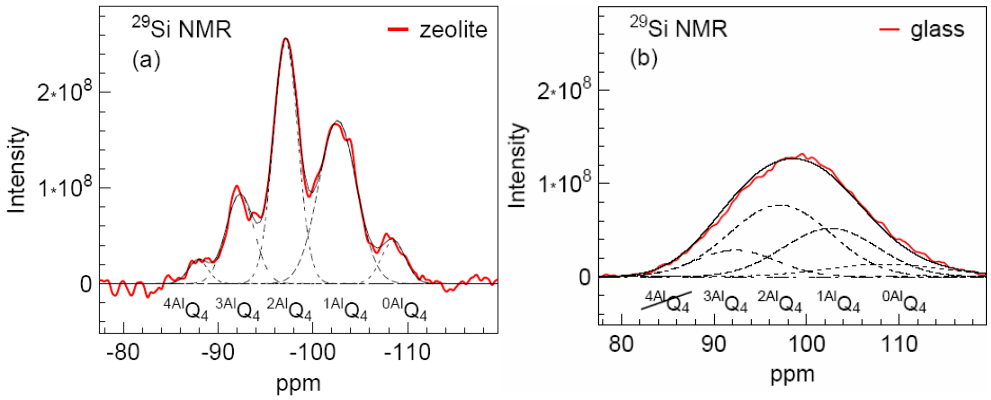

Figure 5. ^{29}Si MASNMR spectra (a) for Na zeolite Y ($Na_{56}Al_{56}Si_{136}O_{384}$) and (b) for the corresponding HDA glass of composition $Na_7Al_7Si_{17}O_{48}$ [32]. The chemical shifts of $^{nAl}Q_4$ tetrahedral species are indicated. The proportions of each are $^{0Al}Q_4$: 6%, $^{Al}Q_4$: 38%, $^{2Al}Q_4$: 37%, $^{3Al}Q_4$: 16% and $^{4Al}Q_4$: 3%.

of the separate resonances for zeolite Y (figure 5(a)), $\Delta\delta$, is 3 ppm, increasing to 12 ppm for the glass (figure 4(b)), reflecting the chemical disorder acquired through amorphization together with topological changes—increases in bond angle disorder amongst bridging oxygens being the most likely source. This is borne out in the *ab initio* computer simulations [15] discussed in section 3, where Si–O–Al linkages are found to be the ones most vulnerable to compressive amorphization.

4.2. Inelastic x-ray scattering

Inelastic x-ray scattering probes a variety of dynamic properties in solids and liquids [39]. These include the (longitudinal) speed of sound, $v_L = \omega_Q/Q$, where ω_Q is the inelastic frequency at x-ray wavevector Q. Given the speed of sound, the longitudinal stiffness coefficient $C_{11} = \rho v_L^2$ can be deduced if the density, ρ, is known. From the ratio of the areas of the elastic (Rayleigh) line and inelastic (Brillouin) doublet—the Landau–Placzek ratio (R_{LP})—static and dynamic inhomogeneities can be contrasted [39]. In particular in the limit $Q \to 0$ the self part of the non-ergodicity factor, f_0, can be equated to the Debye–Waller factor in the harmonic approximation,

$$f_0 = \frac{R_{LP}}{1 + R_{LP}} = e^{-\frac{\langle\mu(T)\rangle^2 Q^2}{3}} \tag{3}$$

where $\langle\mu(T)\rangle^2$ is the mean square displacement of the average atom at temperature T. Figure 6 shows new results made at 600 °C comparing zeolite Y to the melt-quenched HDA glass [40]. Where the zeolite displays the very weakest of Brillouin doublets, inelastic scattering is much stronger for the glass and indeed comparable to measurements published for silica glass [39]. In particular, R_{LP} drops from 15 to 4.6 and f_0 from 0.94 to 0.82 between the zeolite and the glass at 600 °C.

This in turn reflects differences in mechanical rigidity between the microporous crystal and the dense glass which are formally expressed in Poisson's ratio

$$\upsilon_P = \left(\frac{3(B/G) - 2}{6(B/G) + 2}\right) \tag{4}$$

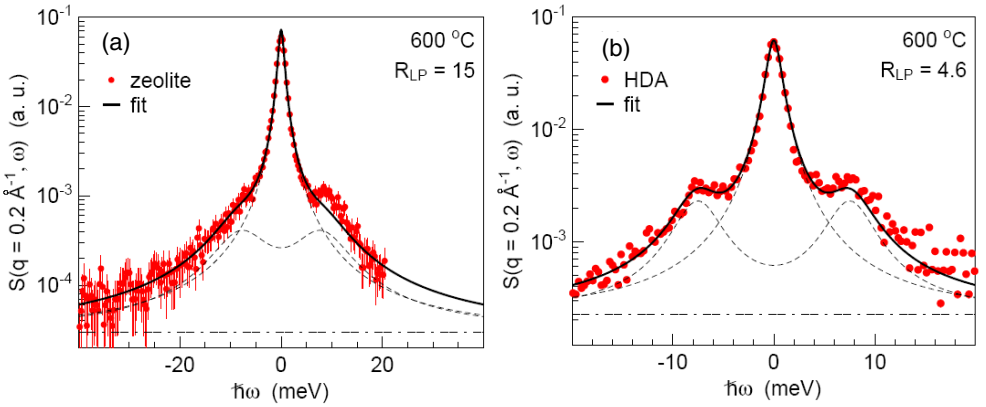

Figure 6. *In situ* inelastic x-ray scattering (a) for Na zeolite Y ($Na_{56}Al_{56}Si_{136}O_{384}$) and (b) for the corresponding HDA glass of composition $Na_7Al_7Si_{17}O_{48}$ measured at $Q = 2$ nm^{-1} on ID16 at the ESRF [40]. Solid curves are fits to the data combining the Rayleigh line, defined by the instrument resolution function, with a symmetrical Brillouin doublet. The ratio of the two areas, the Landau–Placzek ratio (R_{LP}), is 15 for the zeolite and 4.6 for the glass. The speed of sound, $v_L = \omega_Q/Q$, where ω_Q is the inelastic frequency at Q, the x-ray wavevector, is 7.1 km s^{-1} for the zeolite and 5.7 km s^{-1} for the glass.

where $B = (3C_{11} - 4C_{44})/3$ and $G = C_{44}$ are the bulk and shear moduli respectively for isotropic materials. In particular, from the sound velocities, v_L, contained in figures 6(a) and (b), the longitudinal stiffness coefficients, C_{11}, for the zeolite and the HDA glass both turn out to be approximately the same (72.0 ± 0.4 GPa). Taking the bulk modulus, B, for the zeolite Y at ambient pressure from figure 3(b) ($B = \beta^{-1}$) gives a shear stiffness coefficient, C_{44}, of 35 ± 5 GPa, and together yield a Poisson ratio, ν_P, (equation (4)) of 0.02 ± 0.1. The magnitude of ν_P is minute compared to 0.17 for silica or 0.24 for diamond and reflects the superior mechanical rigidity inherent in low density network structures like zeolite Y ($Na_{56}Al_{56}Si_{136}O_{384}$). The errors, however, include the possibility of negative or auxetic Poisson ratios for this cubic microporous structure. The potential for auxetic behaviour in the orthorhombic zeolite natrolite (NAT) $Na_2Al_2Si_3O_{10}$ has recently been speculated from a consideration of its crystallographic elastic constants [41].

We might expect the rigidity of the LDA phase to be intermediate between the zeolite and the HDA glass. To check this out we turn to a remarkable relationship between the fragility, m, of supercooled liquids and the ratio B/G, and hence Poisson's ratio, ν_P, reported by Novikov and Sokolov [42] and shown in figure 7. Fragility simply measures the activation energy of the viscosity, η, at the glass transition, T_g, plotted on a reduced temperature scale T_g/T, namely

$$m = \left(\frac{\mathrm{d}(\log \eta)}{\mathrm{d}(T_g/T)}\right)_{T=T_g}.$$

For example the respective fragilities for the HDA melts measured for zeolite Y and zeolite A are 25 and 40 with glass transition temperatures of 1063 and 1081 K [33]. From figure 7 the fragilities lead to B/G values of 1.3 and 1.7 and Poisson Ratios of 0.20 and 0.27 for HDA glasses with the compositions respectively of zeolite Y ($Na_{56}Al_{56}Si_{136}O_{384}$) and zeolite A ($Na_{12}Al_{12}Si_{12}O_{48}$). By studying the dynamics of zeolite collapse [7] we have derived fragilities, m, for the corresponding LDA melts from zeolite Y and A of 12 and 14 respectively, i.e. significantly less than $m = 20$ for silica, therefore identifying them as super strong liquids [23]. Moreover the T_gs for the LDA liquids are much higher than for the molten

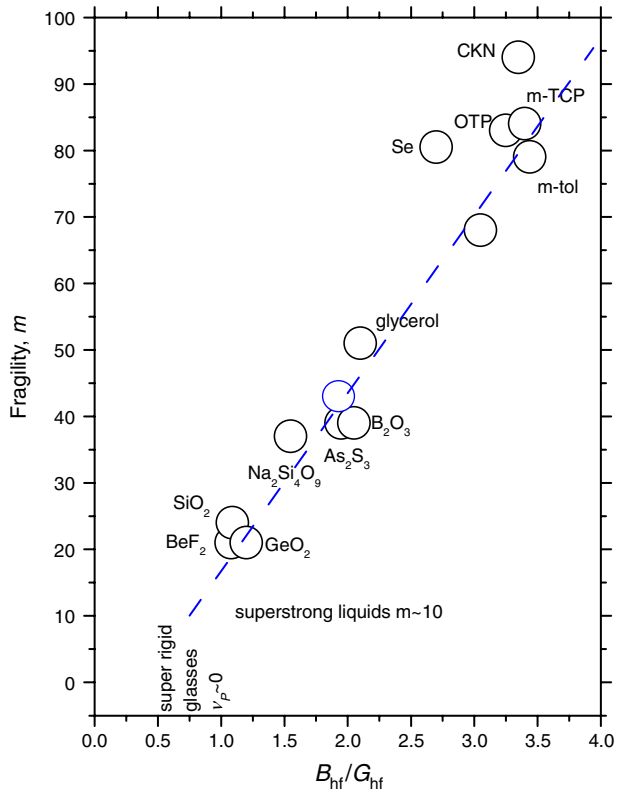

Figure 7. Empirical relationship between the ratio of the high frequency moduli (B_{hf}/G_{hf}) of single-phase glasses and the kinetic fragility, m, of the melts from which they are quenched adapted from [42]. The region of super strong liquids and super rigid glasses is identified where melt fragilities approach $m \sim 10$ [23].

HDA liquids, reaching 1290 and 1203 K for the low density phases derived respectively from zeolite Y and zeolite A [7]. Returning to B/G values from figure 7, these super strong LDA liquids should result in highly rigid glasses [23] with Poisson ratios close to the borderline between positive and negative values given by $B/G = 2/3$ (equation (4)). Indeed for the LDA derived from zeolite Y ν_P turns out to be as low as 0.066 ± 0.9, not as small as the figure of 0.023 obtained from inelastic x-ray scattering for the zeolite (figure 6(a)), but within range of the autectic zone, $B/G < 2/3$. With entropy close to that of zeolite Y, and exhibiting exceptionally high rigidity, LDA phases appear to have many of the chemically ordered and mechanical attributes expected for 'perfect glasses' [43].

5. Amorphization and low frequency vibrations

Displacive phase transitions in silicates—like α to β quartz—can be modelled on the dynamics of low frequency rigid unit modes (RUMs) between adjacent tetrahedra [44]. Equilibrium positions are paired through double-well potentials associated with very soft vibrational modes. In glasses (as well as in some crystalline systems) double-well potentials are asymmetric giving rise to the two-level systems (TLS) with possibilities for tunnelling, which it is now generally accepted as responsible for the unusual low temperature properties of glasses [45]. Moreover,

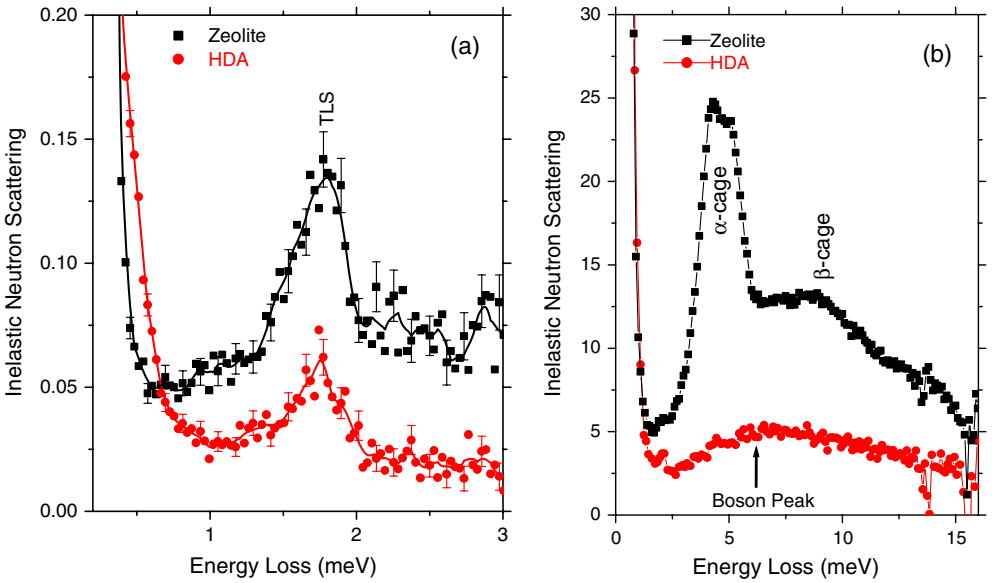

Figure 8. Low frequency modes in Na zeolite Y ($Na_{56}Al_{56}Si_{136}O_{384}$) and glass ($Na_7Al_7Si_{17}O_{48}$) obtained from high resolution inelastic neutron scattering at ISIS on MARI [8]. (a) Bands attributed to librational vibrations from two-level systems in crystalline and HDA phases. (b) Boson Peaks in the zeolite and the glass. The sharp peak in the zeolite has been associated with the large α-cage SBU and the broad peak with the smaller sodalite cages [8]—see figure 1(b).

librational RUMSs in standing wave configurations have been advanced as an explanation for the catalytic activity of metal sites in zeolites [46], following early EXAFS experiments on Ni exchanged zeolite Y [47] where considerable distortion was observed.

5.1. Two-level system (TLS) modes

We have recently detected strong non-dispersed vibrations by inelastic neutron scattering that occur at very low frequencies (4×10^{11} Hz) and low temperatures (10 K) in the tail of the vibrational density of states (VDOS) in zeolites and also in glasses, including silica [8]. These are illustrated in figure 8(a) for zeolite Y and the HDA glass. With increasing temperature the peak position remains constant and the intensity does not scale with the Bose–Einstein function [8]—indicative of the anharmonicity expected from librational modes. More particularly, there is a strong dependence of the intensity of the 400 GHz peak for zeolite Y on the degree of amorphization and therefore on density, which we have used as evidence that these vibrations may be the driving force for destabilizing the microporous cage-like structure, as well as the final conversion to a dense (HDA) amorphous phase [8]. This dependence is illustrated in figure 2, where it is clear that the intensity of the 'librational' feature remains high, during the initial fall in density where the zeolite–LDA transformation is expected. Thereafter the TLS peak falls sharply beyond 50% amorphization where the LDA–HDA transition should occur.

In the *ab initio* computer simulations of pressure induced amorphization of zeolite A [15] discussed in section 3, the displacive II–III transition (figure 4(b)) is characterized by RUMs around corner-sharing tetrahedra, with bond reformations occurring in the topologically disordering III–IV transition—notably associated with the collapse of the double fourfold

rings (figure 3(b)) that link the sodalite cages (figure 1(b)). In addition, these simulated first order transitions in zeolites are found to be reversible, which is consistent with them being driven by librational dynamics. Both transitions involve hysteresis, which is substantial for the topologically disordering III–IV transition which we have associated with the LDA–HDA transformation in figure 4(a). Interestingly we have found experimentally that over protracted periods both thermally induced and pressure induced materials do eventually revert to the crystalline zeolite after persistent annealing around 500 °C. This is close to the temperatures used incidentally for regenerating zeolite catalysts in fluidized bed reactors [1].

5.2. Boson peak

The non-Debye behaviour of glasses at low temperatures is manifest in the specific heat, C_p, which is enhanced above the harmonic C_p/T^3 background of perfect crystals [45]—the same signature occurring in the VDOS$/\omega^2$ [48]. This results in a broad peak—the Boson Peak (BP)—which is typically centred around 1 THz in oxide glasses. Zeolites exhibit a large anomalous specific heat [49] and a huge BP [8] as shown in figure 8(b). Interpretations of the origin of the BP in glasses are numerous [23] so its occurrence in a crystalline system is especially interesting. In particular the BP for zeolite Y exhibits several sharp features whose frequencies can be predicted from the fundamental modes of the large rings that circumscribe the secondary building units of the microporous low density structure (figure 1(b)) and the speed of sound ν_L [8]. For instance the principal peak for zeolite Y in figure 8(b) can be directly related to the large rings that define the α-cage and the broad peak that follows it to the smaller rings that define the sodalite cages.

In a similar way to the TLS feature (figure 8(a)), the BP feature in zeolites shrinks dramatically with amorphization, decreasing sevenfold for 100% amorphization to mirror the size of the BP found in silica [8]. Interestingly partially amorphized material retains both the α-cage and sodalite cage features of the starting zeolite confirming the topological similarity of the initial amorphous phase (LDA or III) evident in figure 4. The dependence of the BP area with amorphization is plotted in figure 2(a) and follows the two-stage reduction in the molar volume, all of which emphasizes the contribution of network topology and density in defining the low frequency VDOS in zeolites as well as oxide glasses in general.

6. Summary of the factors contributing to exothermic amorphization in zeolites

Exothermic compressive amorphization of zeolite A (LTA) and Y (FAU) described in this paper have also been reported for other low density zeolites such as zeolite X [11] and zeolite beta (BETA) [36] and appears to be a general phenomenon for cage-like zeolites. In general collapse temperatures in these materials can be reduced through the presence of large charge-compensating cations like Zn^{2+}, Co^{2+}, Cu^{2+} and Ba^{2+} [1, 50, 51]. For the case of BaA collapse occurs at 450 K close to dehydration with no apparent exotherm [1], but this is likely to be masked by the large endotherm accompanying calcination. In general if water is removed too quickly this can lead to dealuminization (splitting of Si–O–Al connections) which will also reduce collapse temperatures [52, 53].

Whilst thermal amorphization is a characteristic of cage-like zeolites, zeolites constructed from smaller configurations like the S4Rs, S6Rs in phillipsite (PHI) and gismondine (GIS) and the 4–1 units in scolecite (SCO) and natrolite (NAT) are more likely to melt (endothermically) first. These network structures are often higher in density than LTA and FAU and can be amorphized under pressure at ambient temperature [14, 54], but at larger pressures. Along with other feldspar and silicate minerals, Richet and Gillet [16] find that the amorphization

pressure, P_A, increases almost linearly with physical density from around 7 GPa in scolecite to around 60 GPa in $MgSiO_4$. This suggests that $P\Delta V \sim$ constant. The condition for exothermic amorphization, though, seems to rest with the ease with which cage-like microporous structures buckle under thermobaric stress compared to higher density zeolites and silicate minerals. The Poisson ratios are very low and the mechanical rigidity appears to be related to the magnitude of the TLS feature in the low frequency vibrational density of states, illustrated in figure 8(a) for zeolite Y.

Acknowledgments

Jorge Íñiguez, Alexandra Navrotsky, Sabyasachi Sen, Jon Taylor and Martin Wilding are thanked for stimulating discussions. The support of the Higher Education Funding Council of Wales is acknowledged through the Centre for Advanced Functional Materials and Devices, as is the Science and Technology Facilities Council for providing access to the SRS, ESRF and ISIS.

References

[1] Dyer A 1988 *Introduction to Zeolite Molecular Sieves* (New York: Wiley)
[2] Cusmano J A 1992 *Chemtech* **22** 482
[3] Thomas J L, Mange M and Eyaud C 1971 *Molecular Sieve Zeolites—1* (*Advances in Chemistry Series* vol 101) (Washington, DC: American Chemical Society) p 443
[4] Corbin D R, Parise J B, Chowdhry U and Subramanian M A 1991 *Mater. Res. Soc. Symp. Proc.* **223** 213
[5] Subramanian M A, Corbin D R and Chowdhry U 1993 *Bull. Mater. Sci.* **16** 665
[6] Sankar G, Wright P A, Natarajan S, Thomas J M, Greaves G N, Dent A J, Dobson B R, Ramsdale C A and Jones R H 1993 *J. Phys. Chem.* **97** 9550
[7] Greaves G N, Meneau F, Sapelkin A, Colyer L M, ap Gwym I, Wade S and Sankar G 2003 *Nat. Mater.* **2** 622
[8] Greaves G N, Meneau F, Majérus O, Jones D and Taylor J 2005 *Science* **308** 1299
[9] Greaves G N and Meneau F 2004 *J. Phys.: Condens. Matter* **16** S3459
[10] Meneau F and Greaves G N 2005 *Nucl. Instrum. Methods* B **238** 70
[11] Chandrasekhar S and Pramada P N 2002 *Ceram. Int.* **28** 177
[12] Mukhopadhyay A B, Olgschleger C and Dolg M 2003 *Phys. Rev.* B **68** 024205
[13] Mukhopadhyay A B, Olgschleger C and Dolg M 2004 *Phys. Rev.* B **69** 012202
[14] Ovsyuk N and Goryainov S 2006 *Appl. Phys. Lett.* **89** 134103
[15] Peral I and Íñiguez J 2006 *Phys. Rev. Lett.* **97** 225502
[16] Richet P and Gillet P 1997 *Eur. J. Mineral.* **9** 907
[17] Scortinio F, Essmann U, Stanley H E, Hemmati M, Shao J, Wolf G H and Angell C A 1995 *Phys. Rev.* E **52** 6484
[18] Cohen M H, Íñiguez J and Neaton J B 2002 *J. Non-Cryst. Solids* **307–310** 602
[19] Colyer L M, Greaves G N, Carr S W and Fox K K 1997 *J. Phys. Chem.* B **101** 10105
[20] Greaves G N, Meneau F, Majérus O, Jones D and Taylor J 2005 *Science* **308** 1299
[21] Wilding M C, Wilson M and McMillan P F 2006 *Chem. Soc. Rev.* **35** 964
[22] Ponyatovsky E G and Barkolov O I 1992 *Mater. Sci. Rep.* **8** 147
[23] Greaves G N and Sen S 2007 *Adv. Phys.* **56** 1
[24] Götze W 1999 *J. Phys.: Condens. Matter* **11** A1
[25] Kauzmann W 1948 *Chem. Rev.* **43** 219
[26] Hazen R M 1983 *Science* **219** 1065
[27] Lakes R 1993 *Nature* **361** 511
[28] Stanley H E, Buldyrev S V, Franzese G, Giovambattista N and Starr F W 2005 *Phil. Trans. R. Soc.* A **363** 509
[29] Debenedetti P G 2003 *J. Phys.: Condens. Matter* **15** R1669
[30] Mishima O, Calvert L D and Whalley E 1984 *Nature* **310** 393
[31] Mishima O 1994 *J. Chem. Phys.* **100** 5910
[32] Meneau F 2003 Studies of amorphisation in zeolites *PhD Thesis* University of Wales, Aberystwyth
[33] Toplis M J, Dingwell D B, Hess K-U and Lenci T 1997 *Am. Mineral.* **82** 979
[34] Navrotsky A and Tian Z-R 2001 *Chem. Eur. J.* **7** 769

[35] Piccione P M, Laberty C, Yang S, Camblor M A, Navrotsky A and Davis M E 2000 *J. Phys. Chem.* B **104** 10001
[36] Sun P, Deore S and Navrotsky A 2007 *Micropor. Mesopor. Mater.* **98** 29
[37] Lowenstein W 1954 *Am. Mineral.* **39** 92
[38] Lutz W, Ruscher C H and Heidmann D 2002 *Micropor. Mesopor. Mater.* **55** 193
[39] Sette F, Krisch M H, Masciovecchio C, Ruocco G and Monaco G 1998 *Science* **280** 1550
[40] Greaves G N, Meneau F, Kargl F, Ward D and Abergamo F 2007 in preparation
[41] Grima J N, Gatt R, Zammit V, Williams J J, Evans K E, Alderson A and Walton R I 2007 *J. Appl. Phys.* **101** 086102
[42] Novikov V N and Sokolov A P 2004 *Nature* **431** 961
[43] Navrotsky A 2003 *Nat. Mater.* **2** 571
[44] Dove M 1997 *Am. Mineral.* **82** 213
[45] Phillips W A 1981 *Amorphous Solids: Low Temperature Properties* (Berlin: Springer)
[46] Hammonds K D, Deng H, Heine V and Dove M T 1997 *Phys. Rev. Lett.* **78** 3701
[47] Dooryhee E, Steel A T, Maddox P J, Thomas J M, Catlow C R A, Couves J W, Greaves G N and Townsend K P 1991 *J. Phys. Chem.* **95** 1229
[48] Courtens E, Foret M, Hehlen B and Vacher R 2001 *Solid State Commun.* **117** 187
[49] Boerio-Goates J, Stevens R, Lang B and Woodfield B F 2002 *J. Therm. Anal. Calorimetry* **69** 773
[50] Colyer L M, Greaves G N, Dent A J, Fox K K, Carr S W and Jones R H 1995 *Nucl. Instrum. Methods Phys. Res.* B **97** 107
[51] Colyer L M, Greaves G N, Carr S W and Fox K K 1997 *J. Phys. Chem.* B **101** 10105
[52] Lutz W, Fahlke B, Lohse U and Siedel R 1983 *Chem. Technol.* **35** 250
[53] Lutz W, Engelhardt H, Frichner-Scmittler H, Peuker Ch, Löffler E and Siegel H 1985 *Cyst. Res. Technol.* **20** 1217
[54] Gillet P, Malézieux J-P and Itié J-P 1996 *Am. Mineral.* **81** 651